

Numerical Modeling of Ductile Fracture Behavior in Aluminum Weldments

Use of advanced material models makes it possible to predict the ductility and fracture behavior of aluminum weldments

BY M. HVAL, C. THAULOW, J. H. LANGE, S. H. HØYDAL AND Z. L. ZHANG

ABSTRACT. The present investigation focuses on the application of micro-mechanical material modeling by means of the modified Gurson model to determine the deformation and fracture behavior of aluminum weldments. In order to predict the material behavior, a set of material parameters associated with formation and coalescence of voids was established for the different zones in a weld. The material parameters of various positions in the heat-affected zones were determined for two different aluminum alloys, one 6005 alloy and one 6082 alloy, using weld thermal simulated material. The results from numerical simulations of welded wide plates showed that the deformation and fracture characteristics can be predicted fairly well by using the established damage mechanics methodology.

Introduction

The strength and overall deformation characteristics of an aluminum weldment are determined by a number of factors, such as the mechanical properties of the base material and the weld metal, the width of the softened heat-affected zone, the presence of possible welding discontinuities and the local geometry of the joint. This has been demonstrated for aluminum weldments in Refs. 1–3. While the various design codes for aluminum structures specify the minimum recommended strength level to a certain fraction of the base material strength, determined by the β -factor of the joint, little attention is paid to the deformation ability of an aluminum weldment. The deformation ability may be of vital importance for the structural integrity of an aluminum structure subjected to a critical load case. As a consequence of the

soft weld zone in an aluminum weldment the plastic strains tend to localize at the weld. On a global scale, the deformation behavior may be experienced as "elastic," even if the deformations on a local scale are high and the fracture type on the micro scale is ductile.

The finite element method is a tool to determine the deformation behavior of an ideal weldment. With material data such as the true stress-strain curves for the different zones in the weldment, the global deformations can be modeled. However, the incident of fracture is not taken into consideration by any conventional material models used in connection with commercial finite element method codes.

In order to predict the fracture behavior of a welded joint, the real microscopic fracture process also has to be modeled. Besides the theories developed by Rice and Tracey (Ref. 4) and McClintock (Ref. 5), the most successful approach for modeling the nucleation, growth and coalescence of microvoids originating from inclusions and second-phase particles in an elastic-plastic matrix material was developed by Gurson (Ref. 6) and later modified by Tvergaard (Ref. 7). The mathematical background of the model is detailed in Appendix A.

The aim of the present investigation

has been to develop a methodology for determining the fracture behavior of aluminum weldments by means of damage mechanics using the modified Gurson model. Therefore, a detailed characterization of the material properties of the various zones in a weldment has been carried out by using weld thermal simulation. Numerical simulation of the tensile tests was carried out to establish local fracture parameters. As a verification of the methodology, full-size tensile testing of welded wide plates was also simulated by damage mechanics in order to predict the fracture event.

Material Characterization

The present investigation has concentrated on application of damage mechanics on two types of extruded 6xxx-alloys — one 6005 alloy and one 6082 alloy. Both alloys were specially made for detailed fracture and damage mechanics investigations. The materials were cast into 400-mm-diameter extrusion billets and extruded into 150 x 80 mm rectangular hollow sections with wall thickness of 8 and 15 mm and flat 15 x 300 mm plate profiles in a 4000-ton commercial extrusion press. Chemical composition of the two alloys is shown in Table 1.

The mechanical properties of the two materials in the longitudinal and the transverse direction are given in Table 2. Both alloys had a fibrous grain structure that can also be recognized by the clear difference in the longitudinal and transverse tensile properties.

To model the fracture development of the present materials, it is essential to determine the particle size and distribution. These data are important for the nucleation and growth of voids. The particles responsible for the void formation are AlFeSi primary particles formed during the solidification process and large unsolved Mg₂Si constituent particles ap-

KEY WORDS

Aluminum
Weldments
Finite Element Modeling
Weld Thermal Simulation
Damage Mechanics
Gurson Model
Deformation Behavior

M. HVAL, C. THAULOW, J. H. LANGE, S. H. HØYDAL and Z. L. ZHANG are with SINTEF Materials Technology, Trondheim, Norway.

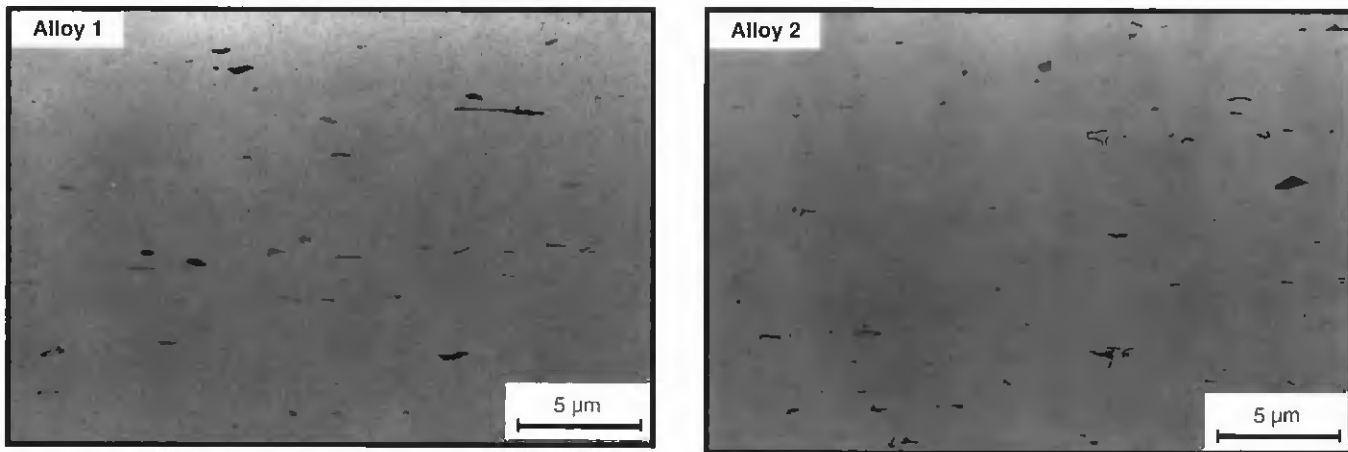


Fig. 1 — Typical particle distribution for the two alloys.

proximately 1 μm in size. After etching, the two types of particles are visible in the microscope as dark (Mg_2Si) and light grey (AlFeSi) particles — Fig. 1. It appeared that, for both alloys, the amount of AlFeSi particles was more or less the same, due to the same amount of Fe, but only Alloy 2 had the Mg_2Si particles. Alloy 2 had a higher content of Mg and Si, and especially the excessive Si content was much higher for this alloy. Quantification of the particle size and distribution was done by semiautomatic image analysis using a Videoplan 2 analyzer. Table 3 summarizes the calculated volume of Mg_2Si and excess of Si and the observed volume

fractions of particles for the two alloys.

In addition to the large particles, a second population of particles — the smaller $\text{Al}(\text{MnCr})\text{Si}$ dispersoids — are important in the last phase of fracture. These particles had an average size of about 0.1 μm and were more or less homogenously distributed in the material. Cr and Mn are added mainly to inhibit recrystallization and control grain size; however, the dispersoids also play an active role in the coalescence between the larger voids. According to Ref. 8, the dispersoids are effective in homogenizing the slip distribution within the grains and thereby also increasing the toughness (Ref. 9).

The exact mechanism of coalescence is not known and no micromechanical parameter can be quantified directly. The coalescence mechanism can only be represented in damage mechanics by the critical void volume fraction, which is more a fitted value than a metallurgically measured quantity.

Weld Thermal Simulation Testing

Weld thermal simulation testing was carried out to determine the local stress-strain relationship for typical positions within the heat-affected zone of the weldment. Rectangular bars with dimen-

Table 1 — Chemical Composition for the Two Alloys

Alloy	Si	Mg	Mn	Cr	Fe
1 (6005)	0.70	0.57	0.24	0.12	0.23
2 (6082)	1.06	0.85	0.24	0.12	0.21

Table 2 — Mechanical Properties of the Two Alloys

Alloy	Longitudinal			Transverse		
	Yield Strength (MPa)	Ultimate Tensile Strength (MPa)	Elongation A ₅ (mm)	Yield Strength (MPa)	Ultimate Tensile Strength (MPa)	Elongation A ₅ (mm)
1 (6005)	294	326	18	279	320	14
2 (6082)	339	371	12	314	361	12

Table 3 — Calculated and Observed Volume Fractions

Alloy	Calculated Volume Fractions of Mg_2Si and Si (%)			Observed Particle Volume Fractions (%)		
	Mg_2Si (Si Required = 0.58 Mg)	$\text{AlFe}(\text{Mn}, \text{Cr})\text{Si}$ (Si Required, 25% of $[\text{Fe} + \text{Mn} + \text{Cr}]$)	Excess of Si = $\text{Si} - \text{Si}_{\text{Mg}_2\text{Si}} -$ $\text{Si}_{\text{AlFe}(\text{Mn}, \text{Cr})\text{Si}}$	$\text{AlFe}(\text{Mn}, \text{Cr})\text{Si}$	Large Mg_2Si	Both
1 (6005)	0.90 (0.33)	(0.15)	0.21	1.34	—	1.34
2 (6082)	1.34 (0.49)	(0.14)	0.43	1.14	0.31	1.44

Numbers in brackets are the Si part.

Table 4 — HV₁ Hardness Values for the Different Simulated Zones

Simulated Zone	Alloy 1 [HV ₁]	Alloy 2 [HV ₁]
HAZ 1 (550°C/932°F)	71	84
HAZ 2 (430°C/806°F)	55	58
HAZ 3 (320°C/608°F)	86	90
HAZ 4 (250°C/482°F)	100	112
base material	110	128

sions 15 × 15 × 180 mm were machined from the profiles in the extrusion direction. The simulation was performed using a Gleeble 2000 weld thermal simulator. Four different thermal programs were performed with peak temperatures of 500°, 430°, 320° and 250°C (932°, 806°, 608° and 482°F, respectively) to simulate the following zones in the HAZ:

- Dissolution tempered and rapidly cooled zone close to the weld interface (550°C/932°F)
- Heavily overaged, forming softest part of the HAZ (430°C/806°F)
- Overaged (320°C/608°F)
- Slightly overaged (250°C/482°F)

Hardness measurements, HV₁, were taken of the simulated material and compared with the real weldments to identify which parts of the HAZ were represented by the simulated material. The hardness values of the different simulated zones in the HAZ are given in Table 4. In Fig. 2, the hardness profiles for the weldments are shown together with the approximate positions for the various weld thermal simulations.

Five-millimeter-diameter tensile specimens were machined from the weld simulated material. In addition, tensile specimens were made from the weld metal of the real weldment. Since the weld metal was of the same type for all the weldments (5183) and the solubility with the base metal is rather small for GMA welding (about 20%), it was assumed that the mechanical properties of weld metal for both weldments were more or less identical. Therefore, only the weld metal from one of the weldments was tested.

The aim of the testing was to determine the material data for the different zones to be used in the numerical simulations. The tensile properties of the different weld simulated zones showed a large variation, especially in the yield stress (Table 5). The true stress-strain curves for the different zones of alloy 1 is shown in Fig. 3. The values after maximum load have been corrected for the stress triaxiality effect according to Bridgeman (Ref. 10). The specimens at the highest peak tempera-

ture were different from the others with a rather low yield stress; however, the hardening rate was significantly higher compared to the others. This is due to the fact that this material had the lowest degree of precipitation hardening since most of the alloying elements (Mg and Si) have gone into dissolution after a heating to 550°C (932°F) with subsequent rapid cooling and no artificial aging.

Even if the fracture type of the tensile specimen in most cases had a dominating shear appearance, areas with a flat fracture type are also observed. Scanning microscope observations indicated clearly that the fracture mechanism was also void of nucleation and coalescence on the apparent shear fractures; hence, the typical dimple-type fracture was dominating on the microscale at least in the central region of the tensile specimens — Fig. 4. Partly intergranular separation was also observed in the transgranular dimpled structure. Since excessive Si tends to precipitate at the grain boundaries, this type of fracture was slightly more evident on alloy 2 than alloy 1.

Establishment of Local Fracture Criteria

To be able to simulate fracture of a weldment by means of damage mechanics, the micromechanical parameters

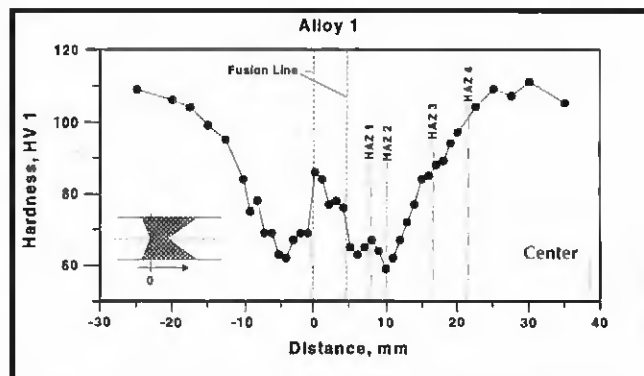


Fig. 2 — Hardness profile for the alloy 1 weldment and the positions for the weld thermal simulations.

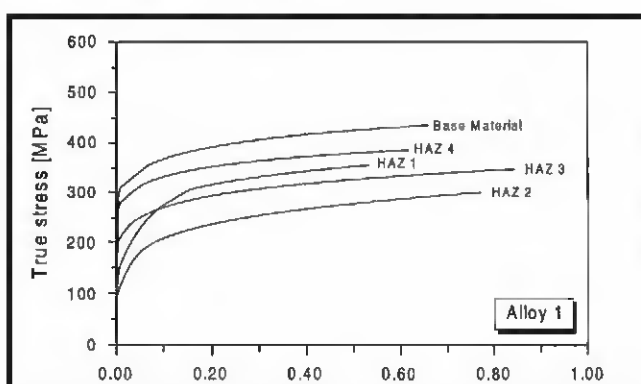


Fig. 3 — True stress-strain curves for the different weld thermal simulated zones of alloy 1.

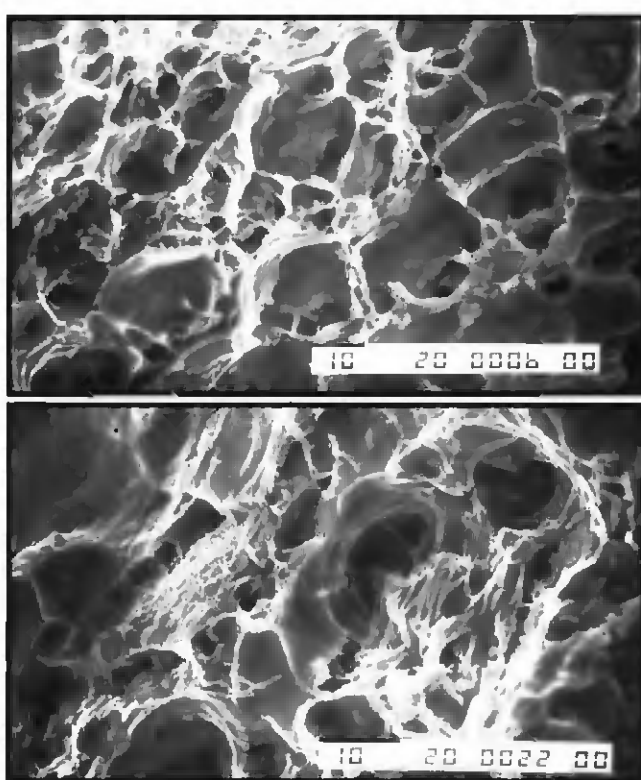


Fig. 4 — Fracture surface observed in scanning electron microscope: A — HAZ 2 of alloy 1; and B — HAZ 2 of alloy 2.

Table 5 — Mechanical Properties of the Different Weld Thermal Simulated Zones, the Base Material and the Weld Metal

Alloy	HAZ Zone	Yield Stress [MPa]		Ultimate Tensile Stress [MPa]		Elongation, A ₅ [%]	
		Test 1	Test 2	Test 1	Test 2	Test 1	Test 2
1 (6005)	HAZ 1	142	139	255	261	20	22
	HAZ 2	88	70	178	185	23	19
	HAZ 3	205	204	240	238	14	13
	HAZ 4	253	273	299	299	14	13
	Base material	317	304	339	331	15	15
2 (6082)	HAZ 1	150	168	275	290	18	18
	HAZ 2	102	104	199	201	17	17
	HAZ 3	226	242	269	284	12	12
	HAZ 4	323	322	343	348	12	11
	Base material	358	356	383	382	13	14
Weld metal	—	—	128	—	278	—	21

HAZ 1: 550°C (932°F)
 HAZ 2: 430°C (806°F)
 HAZ 3: 320°C (608°F)
 HAZ 4: 250°C (482°F)

according to the modified Gurson model must be determined. For this purpose, the experimental load-diameter reduction curves from the tensile tests, measured across the necked section, were used. Numerical simulations were performed for all zones in the weldment for both alloys, in all ten different alloy/heat conditions, in addition to the weld metal, using the true stress-strain curves from the tensile tests. An axisymmetric finite element model was established — Fig. 5. To assure necking in the center region, the diameter of 5 mm was reduced by 0.04 mm. Further, the model consisted of 8-

nodes solid elements, with a condensed element grid in the axial direction near the center of the specimen to detect local changes in the void volume fraction at this location. The analyses were performed in a CRAY YMP computer using ABAQUS finite element code. The modified Gurson model was implemented by using the material subroutine UMAT.

The initial void volume fraction, f_0 , was set equal to zero in this case, assuming that no voids existed in the material before testing. From metallographic examinations, it has been observed that only a part of the particles is active in the

void formation process (Ref. 11), due to their size or shape distribution. Larger particles with irregular shape or high aspect ratio tend to nucleate easier than smaller globular particles. The volume fraction of void nucleating particles, f_N , was therefore set to two-thirds of the volume fraction of the larger particles (AlFeSi or large Mg_2Si), which was in accordance with the observations made in Ref. 11. For alloys 1 and 2, the f_N values were 0.009 and 0.01, respectively. As suggested by Tvergaard (Ref. 18), the parameters q_1 and q_2 were set to 1.5 and 1, respectively. The mean equivalent plastic

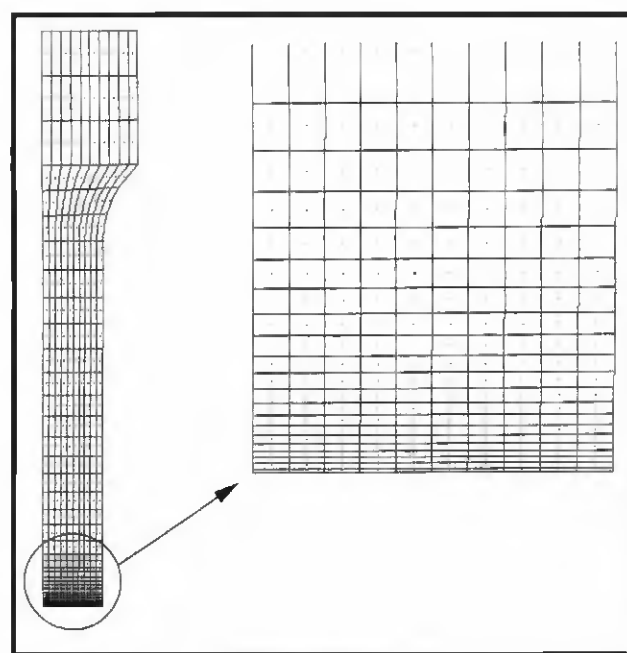


Fig. 5 — The axisymmetric finite element idealization of the tensile specimen.

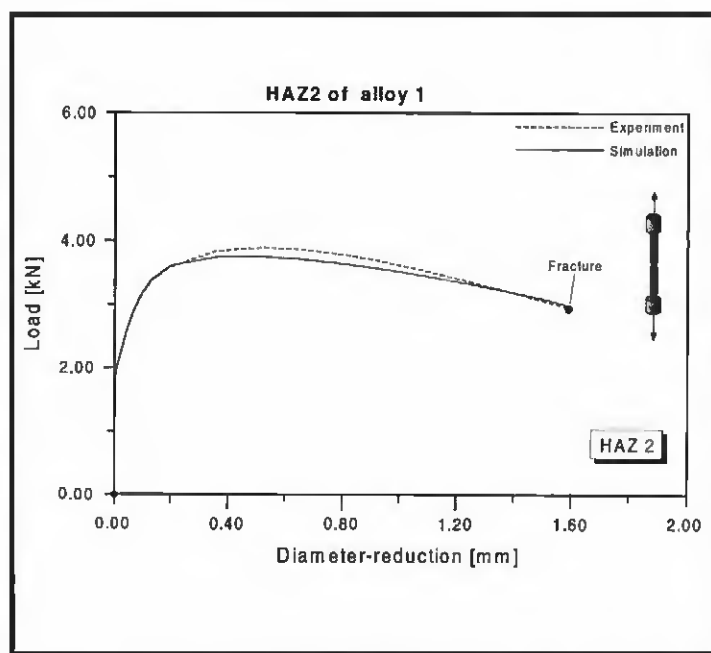


Fig. 6 — Numerical simulation of the tensile test compared with the experiment, test specimen HAZ 2 (430°C/806°F) of alloy 1.

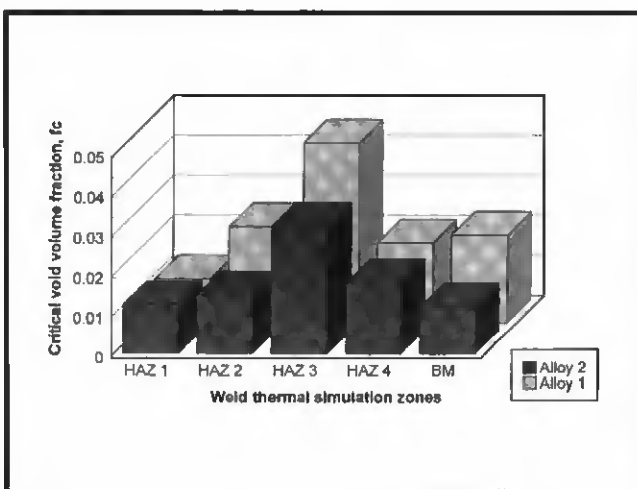


Fig. 7 — Graphical presentation of the critical void volume fraction of the different zones of the weldments.

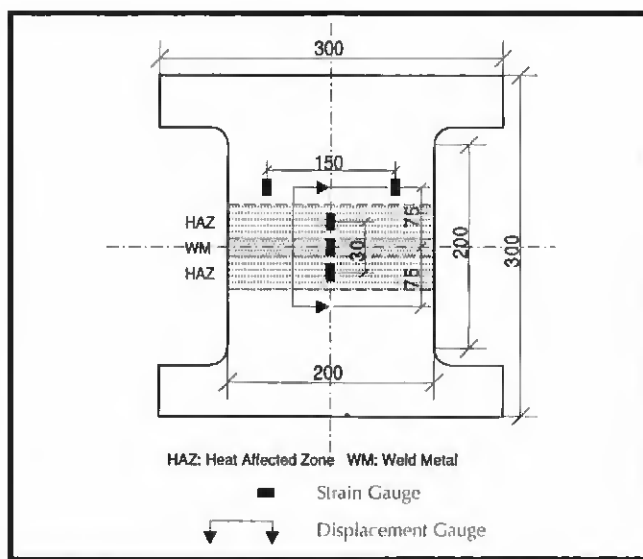


Fig. 8 — Wide plate test dimensions and locations for strain gauges and displacement gauges.

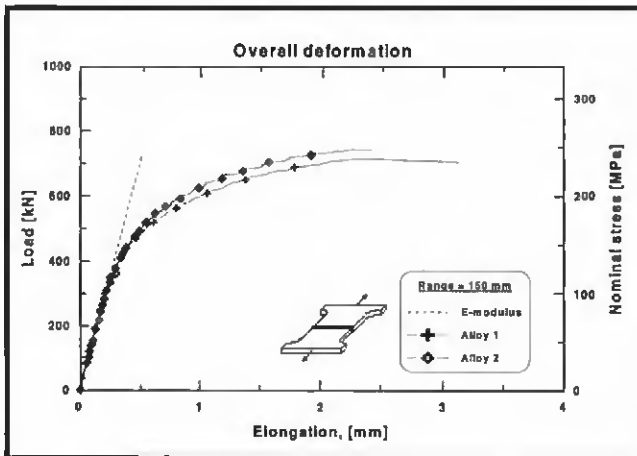


Fig. 9 — Load deformation curves for the weldments of the two alloys.

strain for nucleation of voids, ϵ_{NV} , was set to 0.15 with a standard deviation, s_N , of 0.1. This was in accordance with preliminary observations and experience (Ref. 12). The void volume fraction at final fracture f_f was chosen equal to 0.15. The value of this parameter has, in fact, no significant effect on the numerical results. Since particle shape and distribution with respect to the larger constituent particles and the dispersoids are practically unaffected by the weld thermal cycle, all of the above-mentioned parameters were assumed to be independent of peak temperature of the weld cycle, and therefore the same for all zones in the HAZ.

The critical void volume fraction, f_C — the only remaining variable — was fitted by repeated numerical simulation of the tensile tests to obtain numerical fracture surfaces of both alloys — Fig. 4.

Since the particle distribution of larger

which is the practice used by Sun, et al. (Ref. 13). One example of a simulation is shown in Fig. 6 for HAZ 2 of alloy 1 (peak temperature of 430°C/806°F). The correspondence between the experiment and the numerical simulation is very good, since the two curves coincide both with respect to load-deformation and fracture incident. A similar correspondence was also obtained for the other tensile specimens. The obtained micromechanical parameters according to the modified Gurson model are given in Table 6. The graphical presentation of the critical void volume fraction values of the different zones (Fig. 7) reveals that alloy 2 has significantly lower values for almost all zones in the weld as well as the base material. The reason for the inferior properties of alloy 2 for all temps can be explained by the higher excess of Si in this alloy and the slightly higher volume fraction void nucleating particles. Since Si tends to segregate at grain boundaries Si phase precipitates contribute to the fracture mechanism as a secondary void formation process, giving rise to earlier void coalescence. Evidence for this can be seen when comparing fracture surfaces of both alloys — Fig. 4.

particles and dispersoids is unaffected by the heat cycles, the variation in f_C for the different peak temperatures must be affected by the yield stress level and the hardening rate of the material, which is directly coupled to the dislocation mechanisms controlled by the hardening precipitates. Among the different peak temperatures, HAZ 3 differs from the others with a significantly higher f_C value for both alloys. In this overaged temper ($T_{peak} = 320^\circ\text{C}/608^\circ\text{F}$) the precipitates have grown rather coarse, lost much of their semicoherent strength contribution and approached the size of the dispersoids. In fact, this may also have resulted in additional beneficial effect: homogenizing slip deformation and increasing the fracture resistance in a way similar to that of the dispersoids.

Wide Plate Testing

In order to measure the strength and deformation characteristics of welded connections, wide plate testing was performed. The weld groove was a symmetric K-joint with a groove angle of 55 deg. The welding was performed by means of the pulsed GMAW process. The hardness profiles are shown in Fig. 2. Welded wide plates of both alloys were tested, with dimensions shown in Fig. 8. The width of the welded section was 200 mm. The weld bead reinforcement was machined flat before testing. Three-millimeter-long post yield strain gauges were mounted on both sides of the plate — in the weld metal, in the heat-affected zone 5 mm from the weld interface and in the base material far from the HAZ, to determine

the strain distribution across the weldment. In addition, the overall deformations were measured by means of two displacement transducers mounted on each side of the plate with a gauge length of 150 mm.

The load deformation curves for the weldments of the two alloys are shown in Fig. 9. It appeared that the plastic deformation of both weldments was relatively high, with alloy 1 more ductile than alloy 2, as the load deformation curve for alloy 1 passed beyond the load maximum before fracture occurred. The load capacity for the two weldments, (240 and 247 MPa for alloy 1 and alloy 2, respectively) does not directly reflect the larger difference in tensile properties of the two base materials — Table 2.

The fracture was mainly of "shear" type through the HAZ and the weld metal with the largest part along the softer part of the HAZ. Fracture surface observations by SEM revealed more or less the same fracture types as for the weld thermal simulated tensile specimens. This indicated that weld thermal simulation testing is a reasonable way of studying the fracture mechanisms in aluminum weldments. This is shown in Fig. 10, where the fracture surface micrographs of the heat-affected zones show the distinct difference, as discussed earlier. The fracture surface in the weld metal also clearly shows the typical dimple fracture mode.

Prediction of the Fracture Performance of Weldments

To be able to predict the fracture incident of the two weldments, a finite element idealization of the weldment was made. The model should be representative of the real weld geometry of the wide plates. However, some simplifications were made. The angled side of the groove was the same as the real weldment, 52 deg, and the straight side was perpendicular to the tensile direction. The true weldment did not have a purely straight side, due to the welding procedure — Fig. 11. The ideal form of the weld was kept in the finite element model to detect possible differences in the performance between the two sides. The model (Fig. 12) was a two-dimensional plane strain model made of 1056 4-node elements with reduced integration including six different material data sets — the four sets of material data for the HAZ, the weld metal and the base material. The material data established earlier in this paper were used. The size of the different zones corresponded more or less to the real hardness profiles (Fig. 13); however, some simplifications were made here since the same width of the different

Table 6 — Micromechanical Fracture Parameters for the Different Weld Zones of the Two Alloys

Alloy	Weld Temper	Volume Fraction Void Forming Particles, f_N	Critical Void Volume Fraction, f_C
1 (6005)	HAZ 1	0.009	0.011
	HAZ 2		0.024
	HAZ 3		0.045
	HAZ 4		0.020
	Base material		0.022
2 (6082)	HAZ 1	0.01	0.012
	HAZ 2		0.015
	HAZ 3		0.032
	HAZ 4		0.018
	Base material		0.012
Weld metal	—	0.01	0.0085

zones was used on both sides of the weld through the thickness and for both alloys.

The results from the numerical simulations of the wide plate tests are shown in Fig. 14 compared with the experiments. The predicted performance of the Alloy 2 weldment differs slightly in predicted load compared with the experimental curve; however, the deformation at fracture is quite accurately predicted. For Alloy 1 the predictions deviated more, as the predicted deformation at fracture was significantly higher than that which was experimentally obtained. The deviations will be further discussed in the next section.

Discussion

The reason for the deviation between the experimentally obtained results and the numerical predictions in load performance may be attributed to several different factors. This section discusses the sensitivity of the different factors that may affect the results of the simulations.

The simulations showed a deviation in the load deformation curves that turned out to be slightly nonconservative for both alloys. There are two possible reasons for this. First, the real hardness profile indicated a larger softened zone compared with the finite element idealization. To investigate the effect of width of the soft zones, simulations with two other HAZ widths were performed, one smaller and one larger. The simulations clearly showed that a wider HAZ

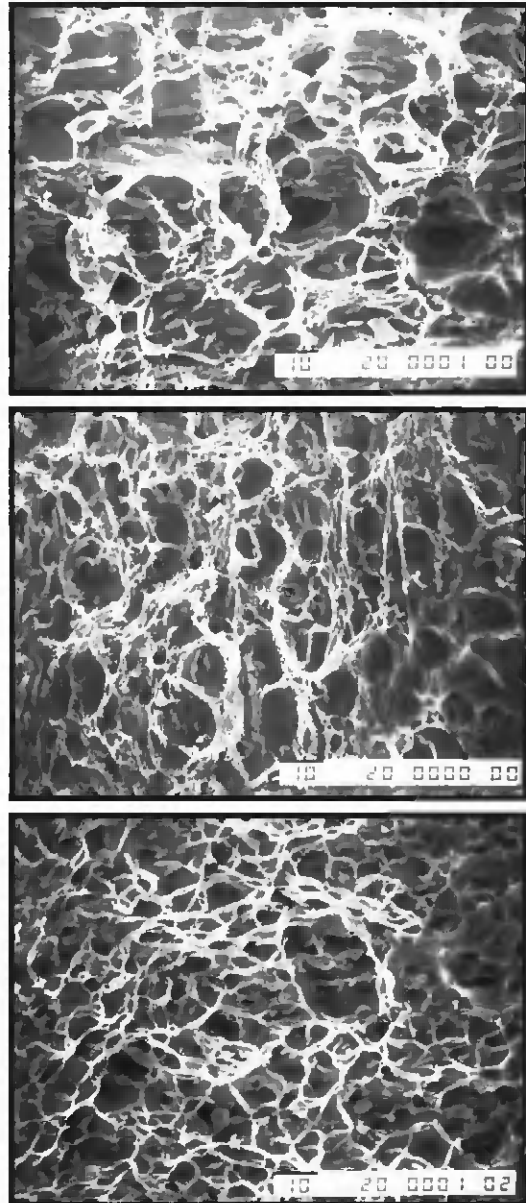


Fig. 10 — Fracture surface of: A — Heat-affected zone of alloy 1; B — Heat-affected zone of alloy 2; and C — Weld metal (alloy 1).

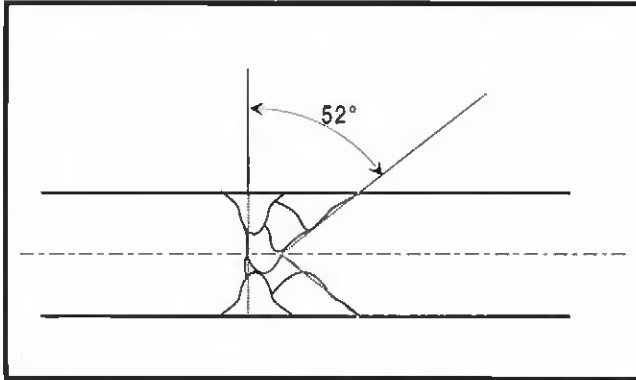


Fig. 11 — Geometry of the real weldment compared to the joint geometry finite element model.

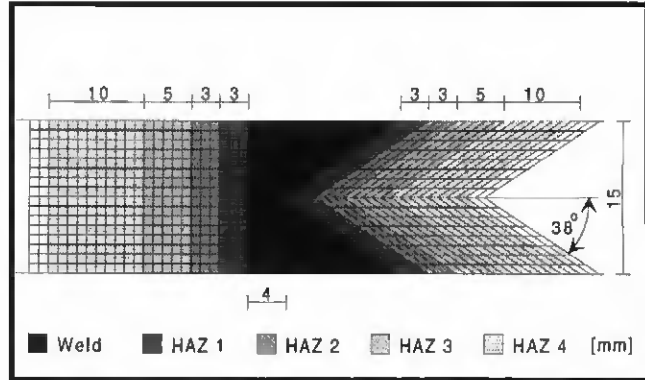


Fig. 12 — The 2-D finite element model of the weldment.

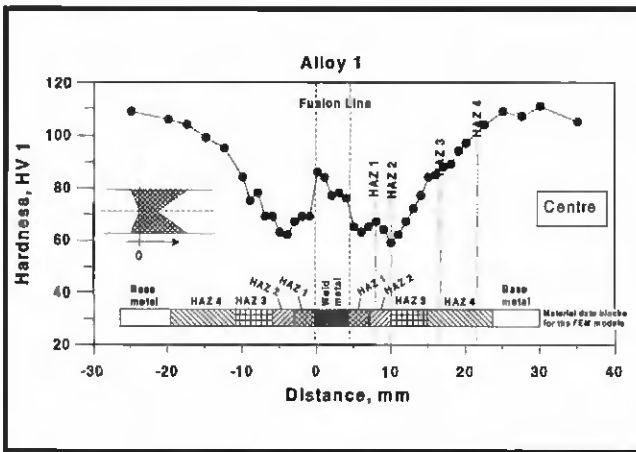


Fig. 13 — The material data blocks compared with the hardness profile.

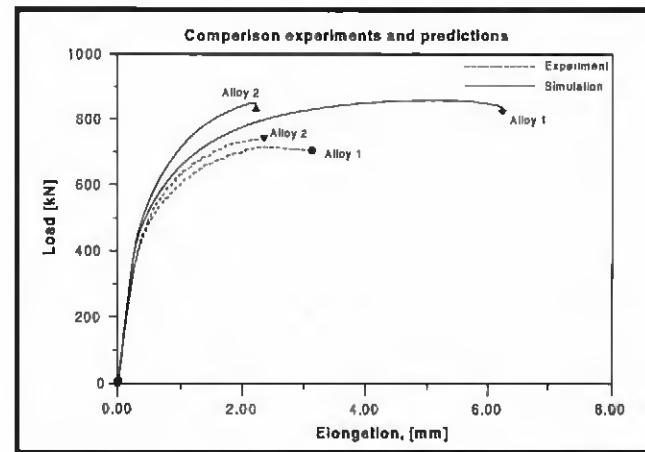


Fig. 14 — Results of numerical simulation of the wide plate tests compared with the experiments.

results in a lower load deformation curve, whereas a smaller width raises the curve — Fig. 15. This is in accordance with earlier observations (Ref. 14). The real size of the zones according to the hardness measurements across the weldments compared with the widths of the models are given in Table 7 and shown graphically in Fig. 16. Here, it appears that the real HAZ width lies between the width of the original (model 2) and the extended model (model 3), which should draw the predicted curve slightly closer to the experimental one. By selecting a case between models 2 and 3, one would lower the curve by 4 and 3% for alloys 1 and 2, respectively. An increase in the HAZ width also slightly delayed the fracture. This is also in accordance with experimental observations (Ref. 15), where welds of thinner plates, with relatively wider HAZ width compared to thicker plates, result in a longer relative elongation at fracture.

Secondly, there is probably also an effect of stress constraint in the numerical simulations. A two-dimensional plane strain model has a stiffer behavior since

the strains are completely constrained in the width direction of the plate. Even though most of the necking at fracture occurred in the thickness direction of the plate, since the plate width was relatively large, some necking was also observed at the edges of the plate. To quantify this possible effect, a corresponding three-dimensional finite element model was generated — Fig. 17. The numerical simulation was performed by standard ABAQUS, without the micromechanical material model, by using the original HAZ widths (model 2). By doing this, the deformation behavior could be predicted, but not the incident of fracture. The results for simulations of alloy 1 showed that the deformation curve is lowered by approximately 5% — Fig. 18.

Taking both of these effects into account by adjusting the predicted load deformation curves by 9 and 8% for alloys 1 and 2, respectively, brings the experiments and the predictions closer together — Fig. 19. For alloy 2 the predictions could not be expected to be better. For alloy 1 the first part of the curve coincides

perfectly; however, the fracture point deviates. It would be too speculative to explain this only by the effect of residual stresses or micro-defects in the weld, even if these factors may have affected the experimental results. It is still a fact that the fracture point after maximum load may be controlled by the loading condition. In the experiment, the loading condition was partly load controlled due to the high elasticity of the loading path giving rise to a more rapid unstable fracture, while the loading in the numerical simulation was displacement controlled.

It should also be mentioned that the "conventional" way of parameter fitting for the Gurson model has been applied in this study. In other words, the nucleation parameters were selected first and the f_C was fitted. Had different values for the nucleation parameters been used, different f_C would have been determined that might also have affected the simulation results. No efforts have been made in this way to improve the simulations.

Finally, it should be mentioned that void nucleation is a complicated process

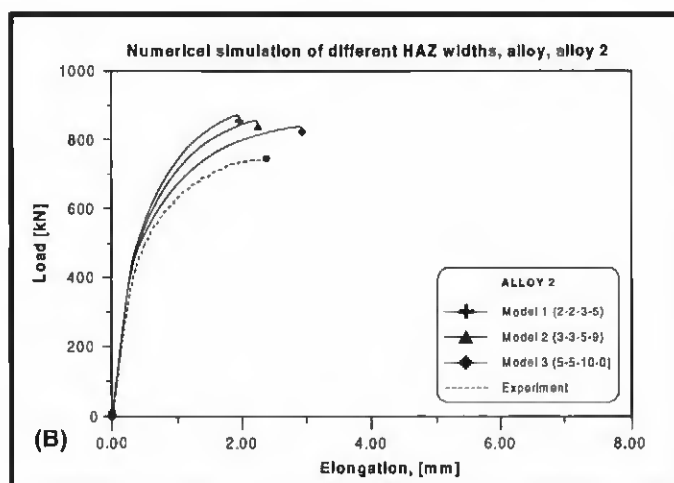
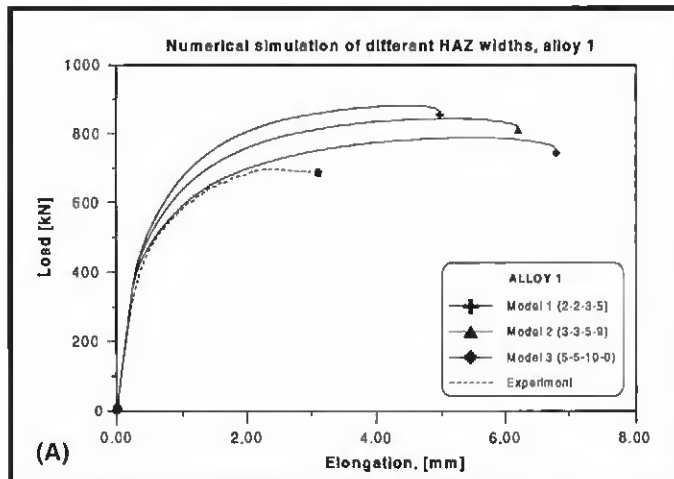


Fig. 15 — Prediction of load deformation behavior for three different HAZ widths compared with experiments. A — Alloy 1; and B — Alloy 2.

in ductile fracture. Thus, proper modeling is a very difficult task in the application of damage mechanics. As far as weldments are concerned, the question of whether the heat cycle affects the nucleation parameters or the critical parameters is not easy to answer. Recently, a new failure criterion for the Gurson model was proposed (Ref. 16), and a methodology for establishing the damage parameters is being developed (Ref. 17). It is argued that by using the failure criterion, which is based on a physical mechanism for void coalescence, the damage parameters can be properly determined. Our further step will be to apply this methodology to the aluminum weldment and compare with the present results.

Conclusions

In this paper, damage mechanics using the modified Gurson model have been applied to aluminum weldments.

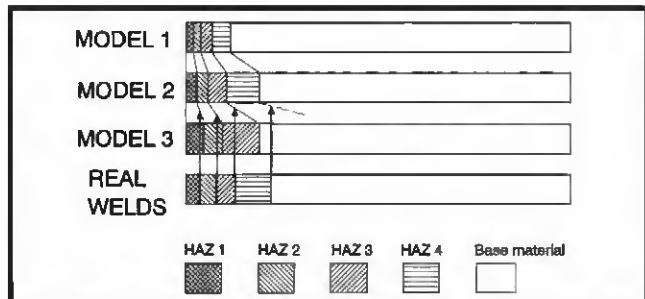


Fig. 16 — HAZ width of the finite element models compared with average of the real weldments.

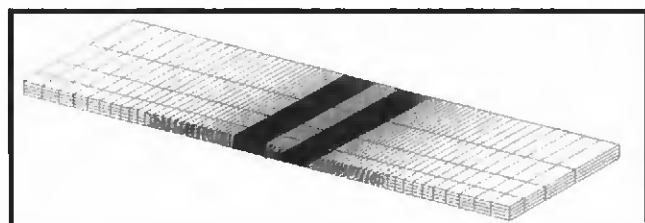


Fig. 17 — Three-dimensional finite element model of the weldment.

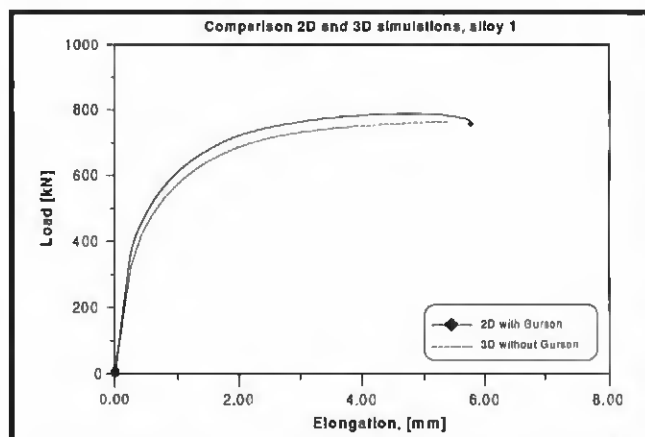


Fig. 18 — The effect of finite width. Comparison between 2-D plane strain and 3-D numerical simulations.

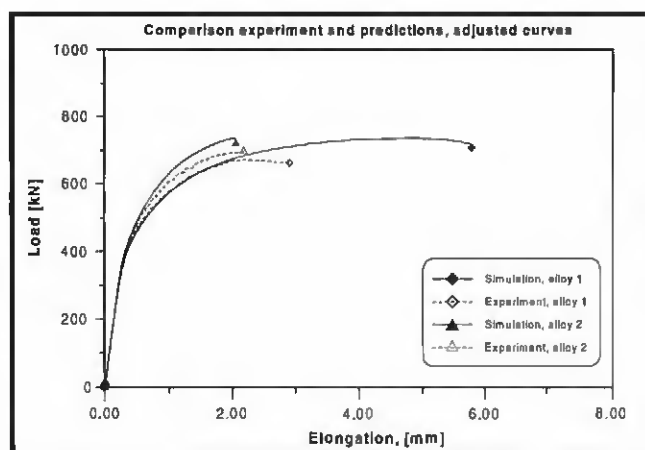


Fig. 19 — Experimental results compared with numerical predictions adjusted for HAZ width and stress condition (2-D plane strain/3-D effect).

Table 7 — Size of the Different HAZ Zones in the Different FE Models and in the Real Weldments

Alloy	Type	HAZ 1	HAZ 2	HAZ 3	HAZ 4
1	Weldment				
	— K-side	5	4	6	10
	— Straight side	3	5	4	12
2	Average	4	4.5	5	11
	Weldment				
	— K-side	5	4	5	10
FEM models	— Straight side	2	4	4	12
	Average	3.5	4	4.5	11
	Model 1	2	2	4	5
FEM models	Model 2 (original)	3	3	5	4
	Model 3	5	5	10	—

the micromechanical parameters for a range of different weld zones if the location of fracture is unknown.

2) The methodology is more or less similar to that for homogenous materials. However, to determine the local HAZ properties one may have to use weld thermal simulated material. It has been demonstrated that HAZ material simulated by a thermal cycle similar to the weld cycle generates material properties equal to the real HAZ of a weld.

3) The critical void volume fraction, f_c , as defined by the modified Gurson model, varied significantly for the different zones in the weld. The lowest values were found in the dissolution tempered zone closest to the weld interface (HAZ 1) and in the base material, while the highest values were found in the overaged zone (HAZ 3). Alloy 1 further showed better properties than alloy 2 for all HAZ zones.

4) The deformation and fracture behavior of welded wide plates could be numerically predicted by means of damage mechanics. Thus, the results served as a verification of the applicability of the methodology. As expected, the predictions were not perfect; however, deviations can be explained by small differences in the weld geometries and the different loading condition in the numerical simulation (displacement controlled) and the experiment (partly load controlled). The predictions also demonstrated the difference in the fracture properties of the weldments of the two alloys, where alloy 1 had significantly better deformation and fracture properties than alloy 2.

Acknowledgments

The authors acknowledge Dr. Dong-Zhi Sun of FhG/IWM in Germany for his valuable assistance with our early FE implementation of the Gurson model. The authors also want to thank the industry

partners of the FAMAL project (Alusingen GmbH, Vereinigte Aluminium Werke AG, Raufoss a.s., Saga Petroleum, Hydro Aluminium and Aker Engineering) for their contribution as well as the Research Council of Norway for its financial support of the present investigation through the EXPOMAT program. And finally, we would like to thank graduate student Espen S. Johansen and the staff at FhG/IWM in Germany for the production of the weld thermal simulated material.

References

- Robertson, I. 1985. Strength loss in welded aluminum structures. Ph.D. thesis. Cambridge University.
- Sølli, O. 1997. Static strength of weldments with soft zones. In Norwegian. Veritas Report No. 77-471.
- Øverås, L., Hval, M., and Thaulow, C. 1992. Mechanical properties of AlMgSi1 weldments and the significance of the softened heat affected zone, 106–112. The 3rd International Conference on Aluminum Alloys, ICAA3, Trondheim, II.
- Rice, J. R., and Tracey, D. M. 1969. On the enlargement of voids in triaxial stress fields. *J. Mech. Phys. Solids* 17: 201–217.
- McClintock, F. A. 1968. A criterion for ductile fracture by the growth of holes. *J. Appl. Mech.* 35: 363–371.
- Gurson, A. L. 1977. Continuum theory of ductile rupture by void nucleation and growth: Part I — Yield criteria and flow rules for porous ductile media. *J. Engng. Mater. Tech.* 99: 2–15.
- Tvergaard, V. 1982. On localization in ductile materials containing spherical voids. *Int. J. Fracture* 18: 237–251.
- Dowling, J. M., and Martin, J. W. 1976. *Acta Metall.* 24: 1147–1153.
- Blind, J. A., and Martin, J. W. 1983. The effect of dispersoids on the ductile fracture toughness of Al-Mg-Si alloys. *Mater. Sci. Eng.* 57: 49–54.
- Bridgman, P. W. 1944. *Trans. Am. Soc. Met.* 32: 553.
- Hval, M. Application of fracture mechanics to the assessment of significance of defects in extruded AlMgSi1 aluminum Alloy. Ph.D. thesis. The Norwegian Institute of Technology, ISBN 82-7119-239-6, NTH 1990: 79.
- Hval, M. Unpublished work.
- Sun, D.-Z., Siegle, D., Voss, B., and Schmitt, W. 1989. Application of local damage models to the numerical analysis of ductile rupture. *Fatigue Fract. Engng. Mater. Struct.* 12(3) 201–212.
- Hval, M., Baur, M., Øvreås, L., and Thaulow, C. 1994. Mismatching effects in the large scale testing of aluminum weldments. *Mismatching of Welds*, eds. K.-H. Schwalbe and M. Koçak. ESIS Publication 17, 709–722, Mechanical Engineering Publication Ltd., London.
- Øvreås, L. Effect of Geometry and width of the soft zone of AlMgSi1 weldments. Ph.D. thesis. Norwegian Institute of Technology, NTH 1994: 120.
- Zhang, Z. L., and Niemi, E. 1995. A new failure criterion for the Gurson-Tvergaard dilational constitutive model. *Int. J. Fracture* 70: 321–334.
- Zhang, Z. L. A methodology for establishing the Gurson parameters. To be published.
- Tvergaard, V. 1990. Material failure by void growth to coalescence. *Advances in Applied Mechanics* 27: 83–151.
- Hancock, J. W. 1982. Plasticity of porous metals. *Yield, Flow and Fracture of Polycrystals*, ed. T. N. Baker, 69–79. Applied Science Puhl.
- Doraivelu, S. M., Gegel, H. L., Guneslera, J. S., Malas, J. C., Morgan, J. T., and Thomas, J. F. 1984. A new yield function for compressible P/M materials. *Int. J. Mech. Sci.* 26: 527–535.
- Becker, R., and Needleman, A. 1986. Effect of yield surface curvature on necking and failure in porous plastic solids. *J. Appl. Mech.* 108: 491–499.
- Becker, R., Needleman, A., Suresh, S., Tvergaard, V., and Vasudevan, A. K. 1987. *An Analysis of Ductile Failure by Grain Boundary Void Growth*. Brown University, Division of Engineering.
- Koplik, J., and Needleman, A. 1988. Void growth and coalescence in porous plastic solids. *Int. J. Solids Structures* 24: 835–853.
- Chu, C. C., and Needleman, A. 1980. Void nucleation effects in biaxially stretched sheets. *J. Engng. Mater. Tech.* 102: 249–256.

Appendix A

Description of the Material Model for Ductile Fracture Behavior

The material model implemented in this investigation is based on the Gurson theory (Ref. 6) modified by Tvergaard (Ref. 7), where the yield function is expressed:

$$\phi = \frac{\bar{\Sigma}^2}{\bar{\sigma}^2} + 2q_1 f \cosh\left(\frac{3q_2}{2} \frac{\Sigma_h}{\sigma_e}\right) - \left(1 + (q_1 f)^2\right) = 0 \quad (1)$$

where Σ is the effective macrostress, Σ_h is

the hydrostatic macrostress, $\bar{\sigma}$ is the yield stress of the matrix material and f is the volume fraction of voids. Both q_1 and q_2 have been introduced to bring the numerical simulations in better agreement with experiments and numerical cell model studies. Tvergaard (Ref. 18) refers to agreement with the equation above for $q_1 = 1.5$ for compacted steel (Ref. 19), $q_1 = 2$ for powder compacted aluminum alloy (Ref. 20), $q_1 = 2.38$ and $q_2 = 0.748$ for porous iron (Ref. 21) and $q_1 = 1.25$ and $q_2 = 0.95$ for sintered iron (Ref. 22). On the basis of these data, a value of q_1 in the range 1.25–2 and $q_2 \approx 1$ can be used. In fact, q_1 seems to be a function of the strain hardening where q_1 increases with decreasing strain hardening (Ref. 23). For q_2 , however, a value of 1 is still the one recommended for most applications.

The first term in Equation 1 expresses the von Mises yield criterion, while the second and third terms represent the loss in load-carrying capacity due to formation of the voids. As can be seen from the equation, the Gurson model itself is not able directly to predict fracture by void coalescence. Instead, a critical parameter for void coalescence, f_C , has to be determined. Once this value is reached, void coalescence occurs and the further fracture development can be modeled. In order to model the correct loss in load-carrying capacity as the void volume fraction increases, f is substituted by f^* :

$$f^* = f, \quad f < f_C \\ f^* = f_C + (f_{UC}(f - f_C)) \quad f \geq f_C$$

where f_C is the critical void volume fraction at void coalescence and f_{UC} is a coefficient for void coalescence dependent on the void volume fraction at coalescence, f_C , and fracture, f_F , and the value of q_1 :

$$f_C = \frac{(f_U^* - f_C)}{(f_F - f_C)}, \text{ where } f_U^* = \frac{1}{q_1} \quad (3)$$

One assumes that both existing voids and nucleated voids contribute to the increase in the void volume fraction. The voids can either exist in the material from the beginning, as an initial void volume fraction, f_0 , or nucleate from fracture of particles or decohesion of the particle/matrix interface at a given stress or strain level. As the increase in void volume fraction during a load increment includes both a growth and a nucleation part, \dot{f} can be expressed by:

$$\dot{f} = \dot{f}_{growth} + \dot{f}_{nucleation} \quad (4)$$

$$\dot{f}_{growth} = (1-f)\dot{\eta}_{kk}^p \quad (5)$$

$$\dot{\eta}_{kk}^p = \dot{\eta}_{11}^p + \dot{\eta}_{22}^p + \dot{\eta}_{33}^p \quad (6)$$

$$\dot{f}_{nucleation} = B\left(\dot{\sigma}_e + \frac{\dot{\sigma}_{kk}}{3}\right) + D\dot{\epsilon}_e^p \quad (7)$$

where $\dot{\eta}_{kk}^p$ is the rate of volumetric

plastic strain. Equation 7 indicates void nucleation can be stress controlled ($B \neq 0$) or strain controlled ($D \neq 0$). In this study, strain controlled nucleation has been assumed, which means that $B = 0$. D is calculated according to the rule proposed by Chu and Needleman (Ref. 24):

$$D = \frac{f_N}{s_N \sqrt{2\pi}} \exp\left[-\frac{1}{2}\left(\frac{(\epsilon_e^p - \epsilon_N)}{s_N}\right)^2\right] \quad (8)$$

where f_N is the volume fraction of particles available for void nucleation, ϵ_e^p is the effective plastic strain, ϵ_N is the mean strain for nucleation and s_N is the corresponding standard deviation.

The model requires extensive quantitative material data. The void volume fraction parameters are material parameters that can be measured either by quantitative metallography or selected individually by trial and error to fit the experimental results.